Evidence for condensed-phase methane enhancement over Xanadu on Titan

M. Ádámkovics [a,*], I. de Pater [a], M. Hartung [b], J.W. Barnes [c]

[a] Astronomy Department, University of California, Berkeley, CA 94720, USA
[b] Gemini Observatory, La Serena, Chile
[c] Department of Physics, University of Idaho, Moscow, ID 83844, USA

ARTICLE INFO

ABSTRACT

We present evidence for condensed-phase methane precipitation near Xanadu using nine nights of observations from the SINFONI integral-field spectrograph at the Very Large Telescope and imaging analysis with empirical surface subtraction. Radiative transfer models are used to support the imaging technique by simulating the spectrometer datacubes and testing for variations in both the surface reflectivity spectrum and atmospheric opacity. We use the models and observations together to argue against artifacts that may arise in the image analysis. High phase angle observations from Cassini/VIMS are used to test against surface scattering artifacts that may be confused with sources of atmospheric opacity. Although changes in the surface reflectivity spectrum can reproduce observations from a particular viewing geometry on a given night, multiple observations are best modeled by condensed-phase methane opacity near the surface. These observations and modeling indicate that the condensed-phase methane opacity observed with this technique occurs predominantly near Xanadu and is most likely due to precipitation.

© 2009 Elsevier Ltd. All rights reserved.

1. Introduction

A methane-based meteorological cycle involving clouds and rain has been suspected to occur on Titan since the time of Voyager, when methane was measured by IRIS (Hanel et al., 1981). Pioneering radiative transfer models of the atmosphere (Toon et al., 1989; McKay et al., 1989) were used to interpret these spectra, predicting rain and patchy clouds from 10 to 30 km (Toon et al., 1988). Ground-based measurements at shorter wavelengths supported the presence of clouds and discovered their daily variation (Griffith et al., 1998, 2000). Advances in imaging technologies lead to spatially resolved observations of clouds near the south pole (Brown et al., 2002; Roe et al., 2002), as well as a region of clouds confined to southern mid-latitudes (Roe et al., 2005a). Since the arrival of Cassini it has been possible to resolve complex cloud structures (Porco et al., 2005), measure updraft velocities (Griffith et al., 2005), and identify polar clouds that may be composed of ethane (Griffith et al., 2006).

Global scale precipitation has been suggested using the methane relative humidity profile measured by Huygens (Tokano et al., 2006). While it was first predicted that droplets would evaporate before reaching the surface (Lorenz, 1993), recent models suggest rain can fall to the ground (Graves et al., 2008).

Fluvial channels indicate that a liquid was in contact with the surface at some time (Tomasko et al., 2005).

Near-IR observations in two methane transmission windows (1.6 and 2.0 μm) have been used with radiative transfer models to measure the column of condensed-phase methane on Titan (Ádámkovics et al., 2007). These data revealed a global cloud of solid methane in the 25–35 km altitude range, with an enhancement of opacity on the morning hemisphere that is consistent with methane drizzle. Recently, these results have been called into question using observations made at the Gemini-North telescope with the NIFS spectrometer (Kim et al., 2008).

Here we present measurements over consecutive nights, together with radiative transfer modeling, to show that the signature of increased condensed-phase methane cannot be due to surface reflectivity artifacts as suggested by Kim et al. (2008), and use high (Sun-target-observer) phase angle measurements to rule out phase angle artifacts. We account for the conclusions and analysis of Kim et al. (2008) by quantifying the errors that can arise in the surface subtraction due to noise and bias. Our observations indicate that while precipitation occurs predominantly near Xanadu, it is not solely a morning phenomenon as suggested earlier (Ádámkovics et al., 2007).

2. Observations

Ground-based observations were performed between 2006 December 28 and 2007 March 11 UT with the adaptive-optics

aided integral-field spectrometer, SINFONI (Eisenhauer et al., 2003), at the Very Large Telescope (VLT). The spectrometer uses two sets of 32 stacked mirrors to divide the field of view (FOV) into 32 'slitlets', which are then optically arranged into a single synthetic long slit that is dispersed onto a cryogenically cooled $2\,K \times 2\,K$ Hawaii detector. Each of the 32 slitlets is imaged onto 64×2000 pixels on the detector. We used the 0.8 in $\times$ 0.8 in FOV, corresponding to a pixel scale of 0.0125 in $\times$ 0.025 in, with the H+K grating covering $1.45-2.45\,\mu m$ at a resolving power, $R = \lambda/\Delta\lambda$, of 2000–3400.

Data-reduction follows the SINFONI pipeline (Modigliani et al., 2007). The pipeline includes a reference bad-pixel map, a check for pixels approaching a non-linear detector response, dark current correction, and flat fielding. All of the spectra are distortion (curvature) corrected using standard flats and arc lamps frames, along with wavelength calibration from a reference arc line table. Spectra are interpolated onto a common wavelength grid before reconstruction of the datacube using the slitlet position and slitlet edge tables.

Mosaicking is performed using AO pointing keywords to overlap images to the nearest pixel and then taking the median value for overlapping pixels. Telluric correction is performed with the extracted spectra of standard stars. Flux calibration is performed by normalization to the disk-integrated stratospheric flux from Keck/OSIRIS observations (Ádámkovics et al., 2007), and are reported in units of albedo, I/F. The observation dates and viewing geometries are given in Table 1.

The Visual and Infrared Mapping Spectrometer (VIMS) on the Cassini spacecraft uses a spectral mapping technique (Brown et al., 2004) to assemble images at 352 wavelengths, covering $0.3–5.1\,\mu m$. Channels near 1.6 and $2.0\,\mu m$ can be used for direct comparison with ground-based observations, and provide the opportunity for high phase angle viewing geometries that are not obtainable from Earth. We use VIMS data that are publicly available from the T10 flyby on 2006 January 15 UT. The data are reduced from observed data numbers to units of albedo, I/F, according to Barnes et al. (2007).

3. Radiative transfer model

In order to interpret the observed spectral datacubes, we create a forward model to simulate the flux that is reflected from Titan's atmosphere and surface. Our model incorporates well-established numerical solutions to the radiative transfer (RT) equation (Griffith et al., 1991; Brown et al., 2002; Ádámkovics et al., 2004, 2007) that reproduce near-IR observations exceptionally well. Updates to the model presented in Ádámkovics et al. (2007)

include the treatment of the surface reflectivity; including the specification of a unique surface spectrum for Xanadu, averaging the surface albedo map over the footprint of a pixel in the model, and an explicit fit for converting the observed surface albedo map to a surface reflectivity map that is input to the model (described in Section 3.3). Limitations in current analyses are due to input parameters (e.g., CH_4 opacities, surface albedo spectra, and aerosol scattering) and not the numerical methodology or assumed geometry. A two-stream approximation (at small phase angles) or discrete ordinates method (at high phase angles) is used to solve the radiative transfer equation for 16 pseudo-plane-parallel layers from 0 to 200 km altitude (Toon et al., 1989; McKay et al., 1989; Stamnes et al., 1988). We correct for the curvature of the atmosphere with an established geometrical correction (Tran and Rannou, 2004). We use the atmospheric temperature and pressure profiles measured *in situ* by Huygens/HASI (Fulchignoni et al., 2005), which are in excellent agreement (below 200 km) with the Voyager profiles (Lellouch et al., 1989). Starting with the *in situ* measurements of aerosol extinctions made by Hugyens/DISR (Tomasko et al., 2005), we vary the extinction at other locations on Titan to reproduce our observations of the global distributions of haze. The uncertainty of the CH_4 opacity, which is greatest for weak transitions, translates into an uncertainty in both the retrieved surface albedo and to a lesser extent the tropospheric aerosol extinction that is constrained at other wavelengths.

3.1. Gas opacity

The vertical profile of CH_4 mixing ratio measured by Huygens/GCMS (Niemann et al., 2005) is applied globally and the absorption coefficients for CH_4 presented by Irwin et al. (2005) are used to calculate CH_4 opacities. Corrections to these coefficients have been published using the measurements made by Huygens/DISR (Tomasko et al., 2008c), however the corrections do not extend to $2\,\mu m$ and are not applied here. An alternative determination of the CH_4 opacity may be performed with line-by-line calculations that use the very high resolution, high sensitivity, CH_4 spectra of Brown (2005). These data are currently available in the HITRAN database. However, the line strengths for these transitions are only applicable at room temperature, and quantum mechanical assignments of individual CH_4 lines are required before opacities can be calculated at the temperatures applicable to Titan. As described by Brown (2005), assigning these transitions requires considerable laboratory and computational effort.

Other sources of gas-phase opacity in the $2.0\,\mu m$ band include low temperature collision-induced absorption by N_2 and H_2 (McKellar, 1989). The H_2-N_2 collision complex is a significant

Table 1
Observation dates and viewing geometry.

Obs. date (UT)	Airmass	Diameter (arcsec)	Sub-observer point		Sub-solar Point		Phase angle (deg)
			°W Long.	Lat.	°W Long.	Lat.	
2006 December 28	1.31	0.835	22.5	−12.3	26.8	−14.1	4.6[a]
2007 January 28	1.30	0.862	1.6	−13.2	3.1	−13.7	1.6[a]
2007 January 29	1.30	0.863	23.9	−13.2	25.3	−13.7	1.5[a]
2007 January 30	1.52	0.863	48.5	−13.2	49.8	−13.7	1.3[a]
2007 January 31	1.35	0.864	68.3	−13.3	69.5	−13.7	1.3[a]
2007 February 23	1.35	0.864	228.0	−14.1	226.6	−13.4	1.4
2007 March 09	1.41	0.855	186.0	−14.5	183.3	−13.2	3.0
2007 March 10	1.37	0.854	206.5	−14.6	203.7	−13.2	3.0
2007 March 11	1.38	0.853	229.0	−14.6	226.1	−13.1	3.1
Cassini T10	–	–	173.4	0.0	127.8	−18.7	48.5

[a] Sub-solar longitude is greater than sub-observer longitude. For these observations, the sub-solar point is to the left of the center of the disk in the images in Fig. 4.

source of opacity near 2.1 μm, which decreases the observed slope of Titan's spectrum in the 2.0 μm band relative to the 1.5 μm band. Since the magnitude of the observed flux can be roughly mapped onto the altitude where most of the scattered photons originate—that is, regions of weak atmospheric absorption are bright and probe the surface, whereas regions of high gas opacity are dim and probe the upper atmosphere—the gradual variation in the 2.0 μm band extinction facilitates altitude discrimination relative to the 1.5 μm band. This collision-induced opacity is critically dependent on the mixing ratio of molecular hydrogen, which we take to be well mixed throughout the atmosphere at levels of $\sim$0.1% (Samuelson et al., 1997).

3.2. Aerosol haze scattering

Observations at IR wavelengths can be represented by models with an approximated scattering phase function (e.g., a one-term Henyey–Greenstein). When calculating the IR flux reflected from Titan at low phase angles there is, in general, a degeneracy between the aerosol scattering phase function and the extinction. For example, an increase in albedo can result either from a greater aerosol density or aerosols that are more backscattering.

The DISR instrument on Huygens was used to measure the haze extinction profile from 0.5 to 1.5 μm (Tomasko et al., 2005), and our ground-based observations made during probe entry (at 1.5 μm) use these measurements as a benchmark for the extinction near the latitude of the Huygens landing site, 10°S. The cumulative DISR extinction is extrapolated to observations at 2 μm (Ádámkovics et al., 2007). Recently, a parameterization of aerosol scattering in three altitude regimes on Titan has been fit to the DISR data (Tomasko et al., 2008a). The authors propose a model of the wavelength dependence of the scattering phase function that is derived using the DISR data and scattering that is treated with the T-matrix method (Mishchenko et al., 1996). The net solar flux both in Titan's atmosphere and at the surface, calculated using the detailed optical properties and distribution of particles, is in good agreement with the values calculated by McKay et al. (1989) (Tomasko et al., 2008b).

We use a simplified parameterization of the phase function, following McKay et al. (1989). The two-stream methodology we use incorporates the total flux that is scattered in the forward and backward directions. This method is not sensitive to further subtleties in the scattering phase function. For the 1.5 and 2.0 μm windows, a one-parameter Henyey–Greenstein phase function has been adequate for interpreting the observations and has accurately predicted the heat balance in the atmosphere (Tomasko et al., 2008b).

The spatial variation in aerosol density is modeled using the method presented in Ádámkovics et al. (2006). The stratospheric aerosol extinction increases northward at a rate of 0.55% per degree latitude from 45°S up to $\sim$70°N, the highest latitudes observed here. The tropospheric aerosol extinction is uniform below 40 km altitude.

3.3. Surface reflectivity

The surface reflectivity is modeled with the simplest representation that can reproduce both spatial and spectral variations in the observations. We start with a high-resolution cylindrically projected map of the 2.018 μm albedo (Barnes et al., 2007) and re-project it onto a sphere viewed on the plane of the sky, at the instrument plate scale, using the JPL HORIZONS ephemerides. For each detector pixel the albedo map is integrated over the spatial region that corresponds to the polygon enclosed by the corners of that pixel, creating an albedo array, $\alpha_{x,y}$. If the corner of a pixel is

located off the edge of the disk then the region of the albedo map that is enclosed by the remaining three corners is used.

Since the observed 2.018 μm albedo has a contribution from atmospheric scattering, it would be a mistake to use $\alpha_{x,y}$ as the input for the surface reflectivity, $R_{x,y}$, in the model. This would result in an overestimate of the flux at surface-probing wavelengths. We use a linear scaling and offset of the entire map to convert from albedo to reflectivity,

$$R_{x,y} = \alpha_{x,y} p_1 + p_2, \tag{1}$$

where the parameters are determined by fitting the output model spectrum to the observations. A series of models are calculated over a range of input values for p_1 and p_2. In each case the mean squared residual between the model and observations is calculated over the entire datacube, and the parameter combination corresponding to the model with the smallest residual is selected as the best fit, $p_1 = 0.83$ and $p_2 = 0.02$.

In the radiative transfer calculation we assume isotropic scattering at the surface. As described in Toon et al. (1989), the total upward flux from the surface is the sum of the reflected downward diffuse flux and flux from any other sources, S_{sfc}. At 2 μm, the other relevant source of flux is the reflection of the incident sunlight that reaches the surface, given by

$$S_{sfc} = R_{x,y} \mu_0 \exp(-\tau/\mu_0) \pi F_s, \tag{2}$$

where μ_0 is the cosine of the solar incidence angle, τ is the optical depth of the atmosphere, and πF_s is the incident solar flux.

The Huygens probe measured the surface reflectivity spectrum *in situ* from the visible up to 1.5 μm (Tomasko et al., 2005). At longer wavelengths, remote observations through narrow regions of low methane opacity are only sensitive to portions of the surface reflectivity spectrum. Since a flat spectrum does not reproduce the observations, i.e., the surface reflectivity in the 1.6 μm window is systematically larger than in the 2.0 μm window and the contrast between bright and dark regions is different (Coustenis et al., 2005; de Pater et al., 2006), we incorporate a surface reflectivity spectrum in our model.

We use a set of Gaussian features in the surface spectrum to resolve discrepancies between the calculated albedo and the observations. The surface reflectivity for the model datacube is given by

$$R(x, y, \lambda) = R_{x,y} \prod_{i=0}^{n} (1 - A_i \exp(-(\lambda_{c,i} - \lambda)/\delta\lambda_i)^2), \tag{3}$$

where we call the product term the surface reflectivity scale factor. Each spectral feature, i, is defined by a central wavelength, $\lambda_{c,i}$, line width, $\delta\lambda_i$, and amplitude, A_i, for n features. Values for the Gaussian features are given in Table 2. Three narrow absorptions are used in the base model and (since $R_{x,y}$ is determined at 2 μm) another Gaussian feature is used to represent the increase in reflectivity toward 1.6 μm. It is unclear if these transitions can be uniquely related to the surface composition. The surface

Table 2
Surface reflectivity spectrum features.

Line center, $\lambda_{c,i}$	Line width, $\delta\lambda_i$	Amplitude, A_i	Notes
1.400	0.250	−0.45[a]	Base model
1.505	0.052	0.95	Base model
1.563	0.012	0.55	Base model
1.982	0.035	0.80	Base model
1.605	0.002	0.07	Only near Xanadu
2.065	0.010	0.07	Only near Xanadu

[a] Since $R_{x,y}$ in Eq. (3) corresponds to observations at 2 μm, a negative amplitude is used to represent the increase in reflectivity toward 1.6 μm (Fig. 1).

reflectivity scale factor is fit globally and individual spectra in the observed datacubes are integrated over vast regions covering more than 10^5 km^2.
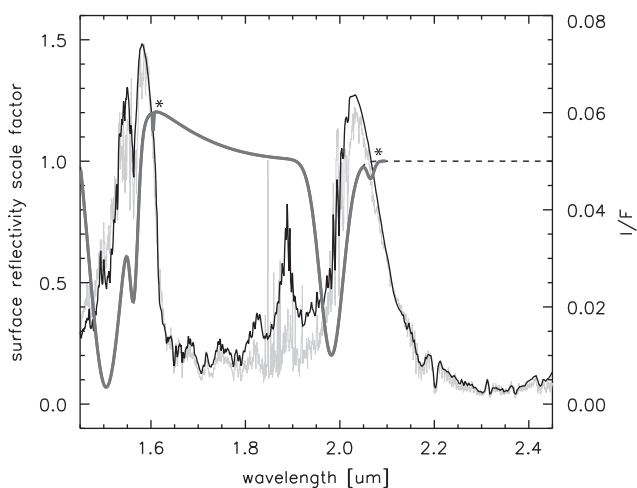
The surface reflectivity scale factor is plotted in Fig. 1 with an example comparison of the model output and observations. By considering the surface reflectivity a free parameter, it is possible to mask uncertainties in atmospheric opacity and fit the spectra arbitrarily well at wavelengths that sense the surface. The relative contribution of surface flux depends on wavelength, surface reflectivity, and viewing geometry. To approximate the fraction of flux arising from the surface in the 2 μm window, we compare a spectrum calculated with the base model to a model spectrum with the surface reflectivity, $R_{x,y}$, set to zero; the two spectra are plotted in Fig. 2. The minimum contribution of the atmospheric flux is 17% of the total, at 2.04 μm for a surface reflectivity of 0.12, and will be larger for lower reflectivity surfaces, and locations near the edge of the disk where the surface is limb-darkened while the atmosphere limb brightens.
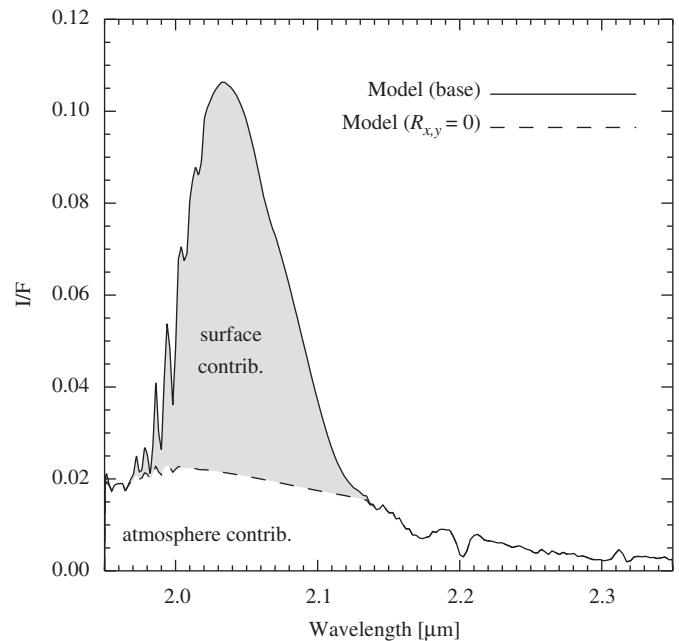
3.4. Condensed-phase methane

After Voyager it was suggested that methane is saturated in some regions of Titan's atmosphere (Flasar et al., 1981; Toon et al., 1988). The methane relative humidity profile measured by Huygens (Fulchignoni et al., 2005) and the presence of clouds both conclusively indicated that methane exists in solid and liquid form in Titan's atmosphere. Despite this evidence, RT models used for direct comparison to near-IR observations have only recently included a rudimentary treatment of condensed-phase methane opacity (Ádámkovics et al., 2007). The morphology of condensed-phase methane (e.g., particles, droplets, or grains) is unconstrained by these models. A solid cloud of methane (Tokano et al., 2006; Ádámkovics et al., 2007) is included in the 25–35 km altitude layer of the model with a methane column volume of 1.5 cm^3 cm^{-2}. The column volume is equivalent to a uniform layer of condensed methane with a thickness, $\ell = 1.5$ cm. The optical depth of condensed-phase methane is given by

$$\tau_c(\lambda) = \ell\alpha(\lambda), \tag{4}$$

where the absorption coefficient spectrum, $\alpha(\lambda)$, is from labora-

Fig. 2. The contribution of flux from the surface in the 2 μm window was calculated by comparing a spectrum of a bright region near the center of the disk in the base model (solid line) with a model that has the surface reflectivity, $R_{x,y}$, set to zero (dotted line). In the case that $R_{x,y} = 0$, all of the flux is from scattering in the atmosphere. The atmospheric scattering is assumed to be the same in the base model, which also includes the light that is reflected from the surface. The maximum surface contribution occurs at 2.04 μm, where the flux from the atmosphere is 17% of the total flux. Integrating the surface contribution over the entire 2 μm window gives a minimum atmospheric contribution of 32% of the total observed albedo.

tory measurements (Grundy et al., 2002). The base model has no additional methane precipitation. This basic treatment of the condensed-phase opacity assumes only absorption and negligible scattering—i.e., the scattering at these altitudes is dominated by aerosol haze.

3.5. Point spread function

The surface reflectivity (from the VIMS albedo map) and the stratospheric aerosol gradient (a free parameter) are the two spatially varying inputs in the model. After these inputs have been determined, the RT calculation of a spectrum is performed for each of the approximately 4000 spatial locations, building a model datacube at the plate scale of the observations. The last step is to convolve the model with a point spread function (PSF). We use the telluric calibration star datacube, collapsed in wavelength across H- and K-bands separately, as the reference images for the PSF. A 2d Gaussian is fit to the PSFs and used as the convolution kernel for each band. Fitting the PSF and then using centered convolution kernel avoids the addition of noise into the model.

4. Surface subtraction

Atmospheric scattering at 2 μm accounts for at least ~17% of the total observed flux, the rest is from the surface. Changes in surface reflectivity at different locations on Titan generally swamp the signal from spatial variations in atmospheric scattering.

Images probing the lower atmosphere are also sensitive to the surface. The latter can be subtracted as described below, to discern atmospheric phenomena (Ádámkovics et al., 2007). We calculate surface subtracted, $\Delta I/F$, images using the method of

Fig. 1. Surface reflectivity spectrum used in RT models is a combination of the surface albedo measured by Cassini/VIMS at 2.018 μm and a wavelength-dependent scale factor (dotted line, left axis). The surface reflectivity spectrum is used to calculate the I/F spectrum (thick line, right axis) and compare to observations (thin line, right axis). The base model surface reflectivity scale factor (dotted line, left axis) fits both the dark and bright regions, and a contrived spectrum with two additional absorptions (indicated near '*') is used only for the region of Xanadu to test the differential imaging analysis.

Ádámkovics et al. (2007) for all of the observations and corresponding models. Each pixel in the subtracted images is defined according to

$$\Delta I/F = (I/F)_{\lambda_1} - f \times (I/F)_{\lambda_2}, \tag{5}$$

where the bandpasses for $(I/F)_{\lambda_1}$ and $(I/F)_{\lambda_2}$ are given in Table 3. The bandpass for $(I/F)_{\lambda_2}$ is selected to cover the wavelength region that probes the surface with the least atmospheric contribution, while $(I/F)_{\lambda_1}$ is integrated over a bandpass with increased methane absorption and therefore contains a larger contribution from the atmosphere. The linear Pearson correlation coefficient, r, between the $\Delta I/F$ image and the $(I/F)_{\lambda_2}$ is determined for a range of f. Surface subtracted images using a range of values for f demonstrate that small values ($f < 0.57$) yield images correlated with surface-probing images, while large values ($f > 0.74$) are anti-correlated with the surface image—that is, they yield and inverted image of the surface albedo pattern and large negative r (Fig. 3). Intermediate values minimize the absolute value of the correlation coefficient. Although the contribution of flux from the surface depends on a reflectivity, the value of f that corresponds to minimum $|r|$ is the optimal value used in this simplistic image subtraction. A single f may be used in a model-independent, approximate method for removing surface albedo variation from images.

Since the background noise in regions of the image with sky can affect the statistical analysis, we performed the calculation of f for each night using only the pixels on the disk of Titan, yielding $\bar{f} = 0.67$, with a mean absolute deviation $\sigma = 0.011$. The scale factors for each night are presented in Table 4 for the 1.5 and 2 μm bands. These values are significantly lower than when the analysis is performed on the entire image, which includes noise from the sky; in that case $\bar{f} = 0.76$ and $\sigma = 0.013$. The values of f calculated while including regions of the sky are consistent with the smallest value calculated by Kim et al. (2008) and larger than $f = 0.72$ used in Ádámkovics et al. (2007). The $\Delta I/F$ images for the observations and all models—each calculated with $\bar{f} = 0.67$—are presented in the bottom four rows of Fig. 4.

Comparison of the observations and the models, in both wavelength regions (λ_1 and λ_2) demonstrates that where the surface albedo is well mapped by Cassini/VIMS, the models reproduce the observations well. Additionally, changes due to additional condensed-phase methane opacity do not produce significant changes to the images in the λ_2 bandpass. The small

Table 3
Bandpasses (μm) used for $\Delta I/F$ images.

|	VLT/SINFONI		Cassini/VIMS[a]
	1.5 μm band	2.0 μm band	2.0 μm band
Surface	1.593–1.596	2.027–2.037	2.026–2.042
Surf. and trop.	1.603–1.606	2.060–2.070	2.059–2.076

[a] Approximated bandpass for individual VIMS channels centered at 2.034, 2.068, 2.117, and 2.150 μm.

Table 4
Surface subtraction parameters.

Obs. date (UT)	1.5 μm band		2.0 μm band	
	f_{best}	$|r|_{min}$	f_{best}	$|r|_{min}$
2006 December 28	0.529	0.0019	0.659	0.0023
2007 January 28	0.550	0.0037	0.667	0.0057
2007 January 29	0.549	0.0052	0.666	0.0014
2007 January 30	0.577	0.0010	0.670	0.0038
2007 January 31	0.581	0.0018	0.684	0.0058
2007 February 23	0.621	0.0024	0.691	0.0027
2007 March 09	0.583	0.0024	0.655	0.0007
2007 March 10	0.606	0.0035	0.686	0.0027
2007 March 11	0.606	0.0046	0.686	0.0040
$\bar{f}_{best}$	0.578		0.674	

Surface
2.027 - 2.037 μm

Lower Troposphere
2.060 - 2.070 μm

2007-01-30 07:42 UT

$f_{best} = 0.670$

$|r|_{min} = 0.0039$

Correlation coefficient, $|r|$

Surface Flux Scaling Factor, f

| $f = 0.570$ | $f = 0.595$ | $f = 0.620$ | $f = 0.645$ | $f = 0.670$ | $f = 0.695$ | $f = 0.720$ | $f = 0.745$ |
| $r = 0.784$ | $r = 0.688$ | $r = 0.535$ | $r = 0.304$ | $r = 0.004$ | $r = -0.297$ | $r = -0.531$ | $r = -0.685$ |
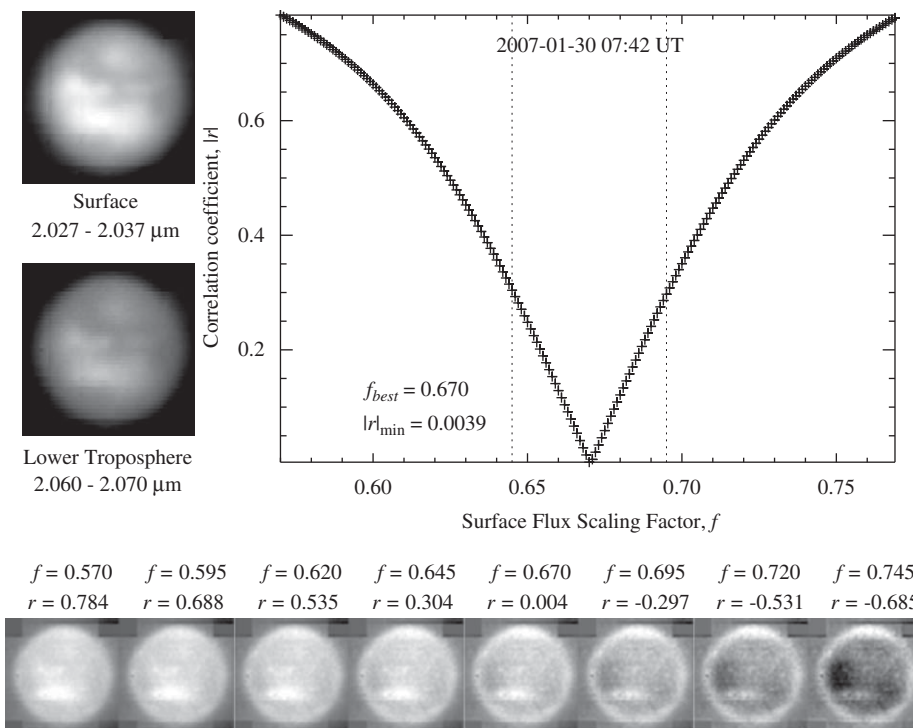
Fig. 3. The scaling factor for the image of the surface flux is determined by an empirical test of the correlation between the surface-probing image and the subtracted image.
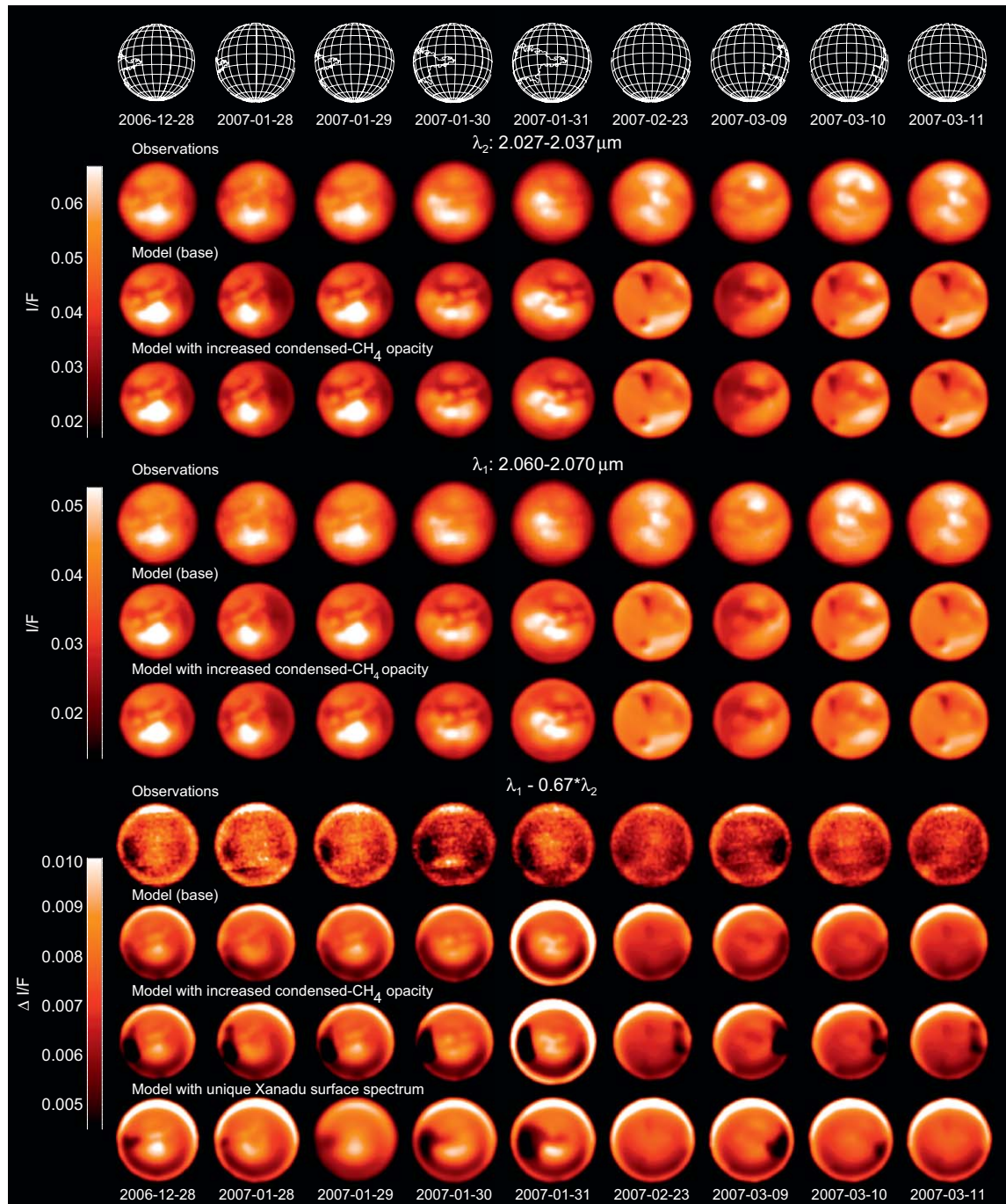
Fig. 4. K-band (2 μm) VLT/SINFONI observations and radiative transfer models both with and without an increase in condensed-phase methane near Xanadu. The increase is modeled to occur from 30°S to 20°N, and from the limb to within 35° of the sub-observer longitude for all observations. A prominent southern mid-latitude cloud (identified at longer wavelengths) contaminates the $\Delta I/F$ image on 2007-01-30 UT, appearing as a bright feature between 30−45°S. An incorrectly high value for f affects areas with the same surface albedo uniformly and would result in all of Titan's bright regions showing small $\Delta I/F$ values. This is not the case here. While Xanadu corresponds to low $\Delta I/F$, other high-albedo surface terrains such as Dilmun (10°N 175°W), Tsegihi (40°S, 35°W), and Adiri (10°S 210°W) do not show similar negative excursions—however, this is not the case for Fig. 3b in Kim et al. (2008).

variations in the flux from subtle changes in opacity and reflectivity are more clearly observed after subtraction of the surface albedo variation. The 1σ pixel-to-pixel noise is between 0.0012 and 0.0016 for all of the observed $\Delta I/F$ images. These values are calculated two ways: first, a conservative estimate is made by calculating the mean of the absolute value of the residuals between the base model and the observations, and second by calculating the FWHM of the histogram of the $\Delta I/F$ values at the center of the disk in each image. In the following discussion, we investigate the suggestion of Kim et al. (2008) that

bright regions of the surface cause artifacts in the difference images.

5. Discussion

The ground-based observations and RT models are presented in Fig. 4. Although the entire observed datacube is calculated (covering $1.45−2.45\,\mu m$) we focus here on images from the

wavelength windows that are used to identify condensed-phase methane opacity.

Kim et al. (2008) argue that anti-correlations are created in $\Delta I/F$ images due to regions of high surface albedo having different f values than dark regions. The argument predicts that bright regions will, in general, be anti-correlated with dark regions in $\Delta I/F$ images. Observations in Fig. 4 demonstrate that a gross anti-correlation does not occur. The brightest regions in the top row of images does not correspond with the dark regions in the subtracted images. Due to limb darkening, regions of the surface with the brightest $(I/F)_{\lambda_2}$ always occur at the center of the disk, whereas dark regions in the $\Delta I/F$ (if present at all) occur near the limb. There is no gross anti-correlation between $(I/F)_{\lambda_2}$ and $\Delta I/F$ images.

Perhaps the argument of Kim et al. (2008) applies only to the region of highest surface reflectivity, Xanadu, or as they suggest, the spectrum of the surface needs to be taken into consideration. The four consecutive nights of observations from 2007-01-28 UT to 2007-01-31 UT are used to test this hypothesis. On 2007-01-28 UT the eastern tip of Xanadu is visible on the limb of Titan, and by 2007-01-31 UT this location is observed at the center of the disk. In the $\Delta I/F$ images from these dates, there is a darker region over the tip of Xanadu on 2007-01-28 UT; however, the same location is no longer dark on 2007-01-31 UT. This sequence of observations suggest that artifacts related to static properties of the surface—which are expected to track with rotation—do not account for the dark regions of the surface. To further test this hypothesis, we employed a systematic change in the surface reflectivity spectrum, but only near Xanadu.

The Xanadu region is outlined (somewhat arbitrarily) using a high resolution ISS map (Porco et al., 2005). A test case is modeled

where the spatial locations in the observed datacubes that are bounded by Xanadu (plotted in the top row of Fig. 4) have two additional surface absorption features, listed in Table 2, and shown graphically in Fig. 1. The features are centered on the wavelength regions that are used to probe the atmosphere, above the surface in both H- and K-bands, and are narrow enough to fit within the λ_2 bandpass used for the images. The effect of this mildly contrived change on the surface-subtracted images is demonstrated in the bottom row of Fig. 4. Not unexpectedly, the region of Xanadu is darker in the difference images. Altering the surface spectrum in such a way could be modified slightly to fit an individual observation very well. However, the series of observations from 2007-01-28 to 2007-01-31 illustrate that a systematic change to the surface reflectivity over Xanadu cannot reproduce all the observations. For these dates, the mean of the absolute value of residuals between the condensed-phase model and the observations is smaller than the residuals of the model with the artificial surface spectrum. On 2007-02-23, 2007-03-10, and 2007-03-11, the models with either additional methane opacity or the surface spectrum change both have larger residuals than the base model.

The observed $\Delta I/F$ image on 2007-01-29 has a darker region near the limb than in the model with a unique Xanadu surface spectrum. This suggests that the absorption spectrum of the Eastern tip of Xanadu is underestimated in the model. However, on 2007-01-31 this same region of Xanadu is near the center of the disk and the absorption spectrum is overestimated in the model. A change to the surface reflectivity spectrum cannot simultaneously match both observations. A similar effect was noted qualitatively in Ádámkovics et al. (2007), and is also illustrated in Fig. 5 with the observations from Kim et al. (2008).
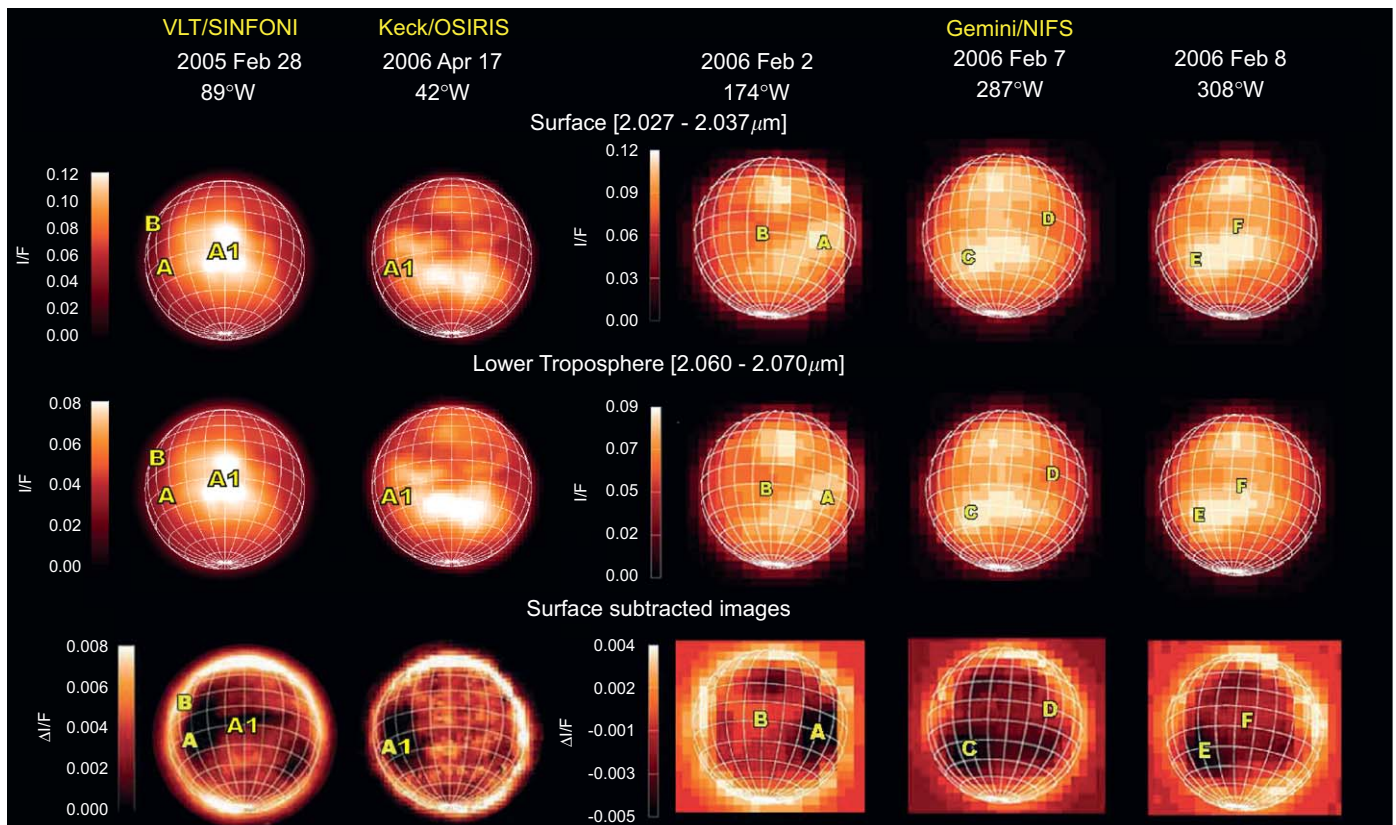

Fig. 5. Comparison of field-integral spectrometer images from three instruments: VLT/SINFONI, Keck/OSIRIS, and Gemini/NIFS. The VLT and Keck data are from Ádámkovics et al. (2007), while with lower S/N and lower resolution Gemini data are combined from Figs. 1 and 3 in Kim et al. (2008). For clarity, the two regions labeled in 'A' by Kim et al. (2008) are separated here as 'A1' and 'A'. The 'A1' regions are dark in the difference image from Keck while appearing bright in the VLT observations.
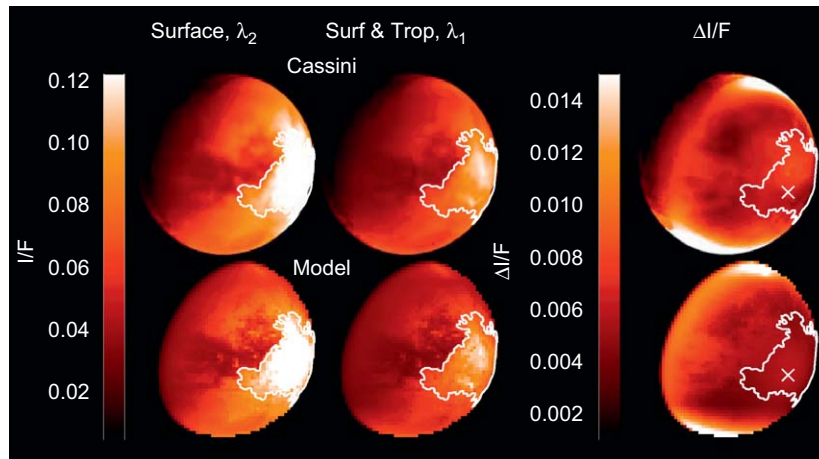
Fig. 6. Cassini/VIMS observations and surface subtracted images at high phase angle (top), with radiative transfer models of the same observing geometry (bottom). The outline indicates Xanadu. Limb brightening in the $\Delta I/F$ images due aerosol scattering is reproduced in the models. Bright scattering at the poles is due to optically thin clouds.

Whereas the two regions of Eastern and Western Xanadu are both labeled 'A' in Figs. 1 and 3 by Kim et al. (2008), here we label the East and West regions separately as 'A' and 'A1', respectively. This clarification shows that while 'A1' is a bright albedo region that shows up as a dark feature in the Keck/OSIRIS difference images from 2006 April 17, this same bright feature—near the center of disk—is no longer a dark region in the difference image viewed with VLT/SINFONI.

We test for surface scattering phase artifacts by performing our analysis on Cassini/VIMS data from the T10 flyby. Since the dark regions in the $\Delta I/F$ images occur near the limb, it is possible that some property of the surface scattering is the cause of an artifact that causes Xanadu to always be dark in the $\Delta I/F$ images near the limb. However, the images in Fig. 6 demonstrate that Xanadu is not an inherently dark region in $\Delta I/F$ images. Intensity variation in the VIMS $\Delta I/F$ image does indicate that a single value of f will not remove all the spatial variation in the subtracted image; however, the gross over-correction for bright regions is avoided for a minimum value of the correlation coefficient, $|r|$. Our RT models also reproduce the high phase angle observations with Lambertian surface scattering and a surface reflectivity scale factor spectrum that does not vary across the disk.

The observations and models presented here can be reconciled with the measurements of Kim et al. (2008) by quantitatively evaluating factors that can affect the determination of f. We calculate f for a subset of pixels in a circle centered on Titan and plot the resultant f as a function of Titan radius, R_T, in Fig. 7. Near the center of the disk ($R_T < 0.7$) , f is roughly constant. There is a decrease in f when limb-darkened regions—where contributions from the surface are small—are included in the correlation analysis. Including regions of the sky adds noise and increases the calculated value of f. We further investigate this effect by systematically adding noise to the images and reproducing our analysis. We generate images with Gaussian noise (of a given FWHM in I/F), add the image of noise to our observations, and then recalculate f (lower scale bar in Fig. 7). Additional noise leads to a systematically higher determination of f (dotted line Fig. 7) such that 1% of additional noise can lead to a increase in f by ~0.02. A linear bias is similarly tested by scaling the $(I/F)_{\lambda_2}$ image (dashed line in Fig. 7). This is an approximation of uncertainties due to flat-fielding, bias-correction, or telluric correction. Both positive or negative deviations in f can occur due to biased images. Data from 2007-01-28 UT are used above for illustration; however, the results generalize to each night of our observations. These tests demonstrate that using the entire
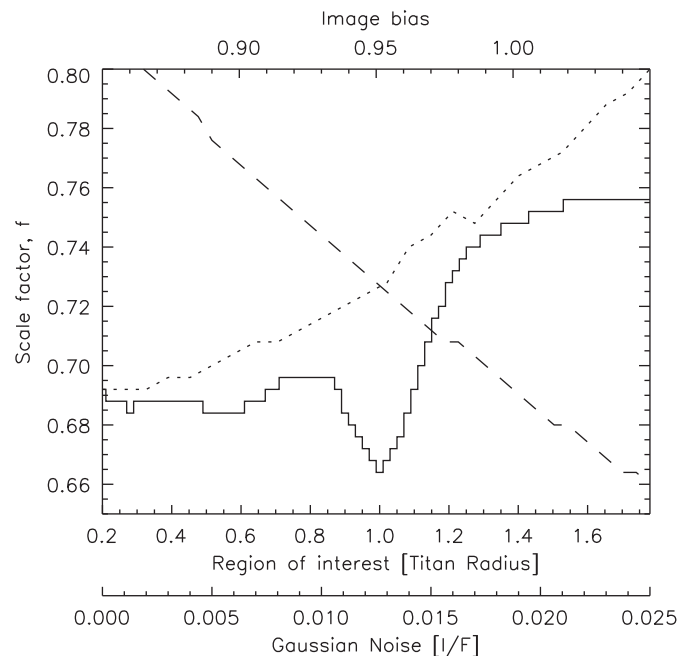
Fig. 7. The optimal surface-subtraction scale factor f depends on the region of interest in the image (solid line, lower axis), bias between the $(I/F)_{\lambda_1}$ and $(I/F)_{\lambda_2}$ image (dashed line, top axis), and the noise in the analyzed images (dotted line, lowest axis). Calculations for bias and noise were made using $R_T < 0.7$.

image in the analysis, an offset during data reduction, or a noisier dataset can all lead to larger values of f, and thus an 'over-subtraction' of the surface. Overestimating f will lead to anti-correlated artifacts from regions of bright surface reflectivity, as detailed in Ádámkovics et al. (2007), and evidenced in Kim et al. (2008). Fig. 5 demonstrates that the Gemini/NIFS data presented by Kim et al. (2008) are noisier than either the VLT/SINFONI or Keck/OSIRIS images presented in Ádámkovics et al. (2007).

6. Conclusions

Atmospheric phenomena are most likely responsible for the observed dark regions in the $\Delta I/F$ images and have been quantitatively reproduced in models using additional con-densed-phase methane (as in Ádámkovics et al., 2007) and tested

here against surface scattering artifacts. Since the extinction properties of haze are not strongly wavelength-dependent in the 2 μm region, spatial variations in haze are removed during the image subtraction and cannot reproduce the dark regions in $\Delta I/F$ images. Altering the haze properties enough to create the dark $\Delta I/F$ regions results in discrepancies that fail to reproduce the observed albedo in tropospheric or stratospheric images (Ádámkovics et al., 2007). Localized meteorology has already been observed (Roe et al., 2005b), so perhaps precipitation is also geographically linked. On 2007-03-09 we observe condensed-phase methane over Xanadu on the evening limb, Fig. 4, indicating that precipitation can occur either in the morning or in the afternoon.

Further modeling of scattering by strongly absorbing droplets or ices is needed to determine if the rain can reach the ground and if there is a predicted signature of rain at longer wavelengths (e.g., 5 μm). There is also a possibility that the condensed methane coexists as a surface coating on aerosols. Alternatively, the optical properties of haze may be such that they mimic methane transmission spectrum, which is unexpected but cannot be ruled out. Currently, enhancement in condensed-phase methane over Xanadu remains the least speculative and the only modeled description of dark regions in $\Delta I/F$ images.

Acknowledgments

References

Ádámkovics, M., de Pater, I., Hartung, M., Eisenhauer, F., Genzel, R., Griffith, C.A., 2006. Titan's bright spots: multiband spectroscopic measurement of surface diversity and hazes. Journal of Geophysical Research (Planets) 111 (10), 7.

Ádámkovics, M., de Pater, I., Roe, H.G., Gibbard, S.G., Griffith, C.A., 2004. Spatially-resolved spectroscopy at 1.6 μm of Titan's atmosphere and surface. Geophysical Research Letters 31 (17), L17S05.

Ádámkovics, M., Wong, M.H., Laver, C., de Pater, I., 2007. Widespread morning drizzle on Titan. Science 318, 962.

Barnes, J.W., Brown, R.H., Soderblom, L., Buratti, B.J., Sotin, C., Rodriguez, S., Le Mouèlic, S., Baines, K.H., Clark, R., Nicholson, P., 2007. Global-scale surface spectral variations on Titan seen from Cassini/VIMS. Icarus 186, 242–258.

Brown, L.R., 2005. Empirical line parameters of methane from 1.1 to 2.1 μm. Journal of Quantitative Spectroscopy & Radiative Transfer 96, 251–270.

Brown, M.E., Bouchez, A.H., Griffith, C.A., 2002. Direct detection of variable tropospheric clouds near Titan's south pole. Nature 420, 795–797.

Brown, R.H., Baines, K.H., Bellucci, G., Bibring, J.-P., Buratti, B.J., Capaccioni, F., Cerroni, P., Clark, R.N., Coradini, A., Cruikshank, D.P., Drossart, P., Formisano, V., Jaumann, R., Langevin, Y., Matson, D.L., McCord, T.B., Mennella, V., Miller, E., Nelson, R.M., Nicholson, P.D., Sicardy, B., Sotin, C., 2004. The Cassini visual and infrared mapping spectrometer (vims) investigation. Space Science Reviews 115, 111–168.

Coustenis, A., Hirtzig, M., Gendron, E., Drossart, P., Lai, O., Combes, M., Negrão, A., 2005. Maps of Titan's surface from 1 to 2.5 μm. Icarus 177, 89–105.

de Pater, I., Ádámkovics, M., Bouchez, A.H., Brown, M.E., Gibbard, S.G., Marchis, F., Roe, H.G., Schaller, E.L., Young, E., 2006. Titan imagery with Keck adaptive optics during and after probe entry. Journal of Geophysical Research (Planets) 111, 7–+.

Eisenhauer, F., Abuter, R., Bickert, K., Biancat-Marchet, F., Bonnet, H., Brynnel, J., Conzelmann, R.D., Delabre, B., Donaldson, R., Farinato, J., Fedrigo, E., Genzel, R., Hubin, N.N., Iserlohe, C., Kasper, M.E., Kissler-Patig, M., Monnet, G.J., Roehrle, C., Schreiber, J., Stroebele, S., Tecza, M., Thatte, N.A., Weisz, H., 2003. SINFO-NI—integral field spectroscopy at 50 milli-arcsecond resolution with the ESO VLT. In: Masanori, I, Moorwood, A.F.M. (Eds.), Instrument Design and Performance for Optical/Infrared Ground-based Telescopes, Proceedings of the SPIE, vol. 4841, pp. 1548–1561.

Flasar, F.M., Samuelson, R.E., Conrath, B.J., 1981. Titan's atmosphere—temperature and dynamics. Nature 292, 693–698.

Fulchignoni, M., Ferri, F., Angrilli, F., Ball, A.J., Bar-Nun, A., Barucci, M.A., Bettanini, C., Bianchini, G., Borucki, W., Colombatti, G., Coradini, M., Coustenis, A., Debei, S., Falkner, P., Fanti, G., Flamini, E., Gaborit, V., Grard, R., Hamelin, M., Harri, A.M., Hathi, B., Jernej, I., Leese, M.R., Lehto, A., Lion Stoppato, P.F., López-Moreno, J.J., Mäkinen, T., McDonnell, J.A.M., McKay, C.P., Molina-Cuberos, G., Neubauer, F.M., Pirronello, V., Rodrigo, R., Saggin, B., Schwingenschuh, K., Seiff, A., Simões, F., Svedhem, H., Tokano, T., Towner, M.C., Trautner, R., Withers, P., Zarnecki, J.C., 2005. In situ measurements of the physical characteristics of Titan's environment. Nature 438, 785–791.

Graves, S.D.B., McKay, C.P., Griffith, C.A., Ferri, F., Fulchignoni, M., 2008. Rain and hail can reach the surface of Titan. Planetary and Space Science 56, 346–357.

Griffith, C.A., Hall, J.L., Geballe, T.R., 2000. Detection of daily clouds on titan. Science 290, 509–513.

Griffith, C.A., Owen, T., Miller, G.A., Geballe, T., 1998. Transient clouds in Titan's lower atmosphere. Nature 395, 575–578.

Griffith, C.A., Owen, T., Wagener, R., 1991. Titan's surface and troposphere, investigated with ground-based, near-infrared observations. Icarus 93, 362–378.

Griffith, C.A., Penteado, P., Baines, K., Drossart, P., Barnes, J., Bellucci, G., Bibring, J., Brown, R., Buratti, B., Capaccioni, F., Cerroni, P., Clark, R., Combes, M., Coradini, A., Cruikshank, D., Formisano, V., Jaumann, R., Langevin, Y., Matson, D., McCord, T., Mennella, V., Nelson, R., Nicholson, P., Sicardy, B., Sotin, C., Soderblom, L.A., Kursinski, R., 2005. The evolution of Titan's mid-latitude clouds. Science 310, 474–477.

Griffith, C.A., Penteado, P., Rannou, P., Brown, R., Boudon, V., Baines, K.H., Clark, R., Drossart, P., Buratti, B., Nicholson, P., McKay, C.P., Coustenis, A., Negrao, A., Jaumann, R., 2006. Evidence for a polar ethane cloud on Titan. Science 313, 1620–1622.

Grundy, W.M., Schmitt, B., Quirico, E., 2002. The temperature-dependent spectrum of methane ice I between 0.7 and 5 μm and opportunities for near-infrared remote thermometry. Icarus 155, 486–496.

Hanel, R., Conrath, B., Flasar, F.M., Kunde, V., Maguire, W., Pearl, J.C., Pirraglia, J., Samuelson, R., Herath, L., Allison, M., Cruikshank, D.P., Gautier, D., Gierasch, P.J., Horn, L., Koppany, R., Ponnamperuma, C., 1981. Infrared observations of the Saturnian system from Voyager 1. Science 212, 192–200.

Irwin, P.G.J., Sihra, K., Bowles, N., Taylor, F.W., Calcutt, S.B., 2005. Methane absorption in the atmosphere of Jupiter from 1800 to 9500 cm^{-1} and implications for vertical cloud structure. Icarus 176, 255–271.

Kim, S.J., Trafton, L.M., Geballe, T.R., 2008. No evidence of morning or large-scale drizzle on Titan. Astrophysical Journal 679, L53–L56.

Lellouch, E., Coustenis, A., Gautier, D., Raulin, F., Dubouloz, N., Frere, C., 1989. Titan's atmosphere and hypothesized ocean—a reanalysis of the Voyager 1 radio-occultation and IRIS 7.7 μm data. Icarus 79, 328–349.

Lorenz, R.D., 1993. The life, death and afterlife of a raindrop on Titan. Planetary and Space Science 41, 647–655.

McKay, C.P., Pollack, J.B., Courtin, R., 1989. The thermal structure of Titan's atmosphere. Icarus 80, 23–53.

McKellar, A.R.W., 1989. Low-temperature infrared absorption of gaseous N$_2$ and N$_2$ + H$_2$ in the $2.0-2.5$ μm region—application to the atmospheres of Titan and Triton. Icarus 80, 361–369.

Mishchenko, M.I., Travis, L.D., Mackowski, D.W., 1996. T-matrix computations of light scattering by nonspherical particles: a review. Journal of Quantitative Spectroscopy & Radiative Transfer 55, 535–575.

Modigliani, A., Hummel, W., Abuter, R., Amico, P., Ballester, P., Davies, R., Dumas, C., Horrobin, M., Neeser, M., Kissler-Patig, M., Peron, M., Rehunanen, J., Schreiber, J., Szeifert, T., 2007. The SINFONI pipeline. ArXiv Astrophysics e-prints.

Niemann, H.B., Atreya, S.K., Bauer, S.J., Carignan, G.R., Demick, J.E., Frost, R.L., Gautier, D., Haberman, J.A., Harpold, D.N., Hunten, D.M., Israel, G., Lunine, J.I., Kasprzak, W.T., Owen, T.C., Paulkovich, M., Raulin, F., Raaen, E., Way, S.H., 2005. The abundances of constituents of Titan's atmosphere from the GCMS instrument on the Huygens probe. Nature 438, 779–784.

Porco, C.C., Baker, E., Barbara, J., Beurle, K., Brahic, A., Burns, J.A., Charnoz, S., Cooper, N., Dawson, D.D., Del Genio, A.D., Denk, T., Dones, L., Dyudina, U., Evans, M.W., Fussner, S., Giese, B., Grazier, K., Helfenstein, P., Ingersoll, A.P., Jacobson, R.A., Johnson, T.V., McEwen, A., Murray, C.D., Neukum, G., Owen, W.M., Perry, J., Roatsch, T., Spitale, J., Squyres, S., Thomas, P., Tiscareno, M., Turtle, E.P., Vasavada, A.R., Veverka, J., Wagner, R., West, R., 2005. Imaging of Titan from the Cassini spacecraft. Nature 434, 159–168.

Roe, H.G., Bouchez, A.H., Trujillo, C.A., Schaller, E.L., Brown, M.E., 2005a. Discovery of temperate latitude clouds on Titan. Astrophysical Journal 618, L49–L52.

Roe, H.G., Brown, M.E., Schaller, E.L., Bouchez, A.H., Trujillo, C.A., 2005b. Geographic control of Titan's mid-latitude clouds. Science 310, 477–479.

Roe, H.G., de Pater, I., Macintosh, B.A., McKay, C.P., 2002. Titan's clouds from Gemini and Keck adaptive optics imaging. Astrophysical Journal 581, 1399–1406.

Samuelson, R.E., Nath, N.R., Borysow, A., 1997. Gaseous abundances and methane supersaturation in Titan's troposphere. Planetary and Space Science 45, 959–980.

Stamnes, K., Tsay, S.-C., Jayaweera, K., Wiscombe, W., 1988. Numerically stable algorithm for discrete-ordinate-method radiative transfer in multiple scattering and emitting layered media. Applied Optics 27, 2502–2509.

Tokano, T., McKay, C.P., Neubauer, F.M., Atreya, S.K., Ferri, F., Fulchignoni, M., Niemann, H.B., 2006. Methane drizzle on Titan. Nature 442, 432–435.

Tomasko, M.G., Archinal, B., Becker, T., Bézard, B., Bushroe, M., Combes, M., Cook, D., Coustenis, A., de Bergh, C., Dafoe, L.E., Doose, L., Douté, S., Eibl, A., Engel, S., Gliem, F., Grieger, B., Holso, K., Howington-Kraus, E., Karkoschka, E., Keller, H.U.,

Kirk, T.P., Kramm, R., Küppers, M., Lanagan, P., Lellouch, E., Lemmon, M., Lunine, J., McFarlane, E., Moores, J., Prout, G.M., Rizk, B., Rosiek, M., Rueffer, P., Schröder, S.E., Schmitt, B., See, C., Smith, P., Soderblom, L, Thomas, N., West, R., 2005. Rain, winds and haze during the Huygens probe's descent to Titan's surface. Nature 438, 765–778.

Tomasko, M.G., Bézard, B., Doose, L., Engel, S., Karkoschka, E., 2008a. Measurements of methane absorption by the descent imager/spectral radiometer (DISR) during its descent through Titan's atmosphere. Planetary and Space Science 56, 624–647.

Tomasko, M.G., Bézard, B., Doose, L., Engel, S., Karkoschka, E., Vinatier, S., 2008b. Heat balance in Titan's atmosphere. Planetary and Space Science 56, 648–659.

Tomasko, M.G., Doose, L., Engel, S., Dafoe, L.E., West, R., Lemmon, M., Karkoschka, E., See, C., 2008c. A model of Titan's aerosols based on measurements made inside the atmosphere. Planetary and Space Science 56, 669–707.

Toon, O.B., McKay, C.P., Ackerman, T.P., Santhanam, K., 1989. Rapid calculation of radiative heating rates and photodissociation rates in inhomogeneous multiple scattering atmospheres. Journal of Geophysical Research 94, 16287–16301.

Toon, O.B., McKay, C.P., Courtin, R., Ackerman, T.P., 1988. Methane rain on Titan. Icarus 75, 255–284.

Tran, T.T., Rannou, P., 2004. Comparing 3D spherical Monte-Carlo and 2-stream parallel plane simulation of far-field backscattering image of Titan. Notes du Pre de Planetologie de l'Institut Pierre Simon Laplace 2, 18–38.